

Journal of Photonics for Energy

SPIEDigitalLibrary.org/jpe

Connecting physical properties of spin-casting solvents with morphology, nanoscale charge transport, and device performance of poly(3-hexylthiophene):phenyl- C₆₁-butyric acid methyl ester bulk heterojunction solar cells

Pavel Dutta
Yu Xie
Mukesh Kumar
Monika Rathi
Phil Ahrenkiel
David Galipeau
Qiquan Qiao
Venkat BommiSETTY



SPIE

Connecting physical properties of spin-casting solvents with morphology, nanoscale charge transport, and device performance of poly(3-hexylthiophene):phenyl-C₆₁-butyric acid methyl ester bulk heterojunction solar cells

Pavel Dutta,^a Yu Xie,^a Mukesh Kumar,^a Monika Rathi,^b Phil Ahrenkiel,^b David Galipeau,^a Qiquan Qiao,^a and Venkat Bommisetty^a

^aSouth Dakota State University, Department of Electrical Engineering, Brookings, South Dakota 57007

venkat.bommisetty@sdstate.edu

^bSouth Dakota School of Mines and Technology, Nanoscience and Nanoengineering Department, Rapid City, South Dakota 57701

Abstract. The correlation between the physical properties of spin-casting solvents, film morphology, nanoscale charge transport, and device performance was studied in poly(3-hexylthiophene):phenyl-C₆₁-butyric acid methyl ester (P3HT:PCBM) blends, spin cast with two halogenated aromatic solvents: chlorobenzene (CB) and ortho-dichlorobenzene (1,2-DCB). 1,2-DCB-based blends exhibited fine phase separation of ~10 to 15 nm length scale with ordered self-assembly of P3HT whereas blends spin cast from CB showed coarse phase separation with large isolated clusters of ~25 to 100 nm of donor- and acceptor-rich regions. Higher solubility of both P3HT and PCBM in 1,2-DCB and a slower drying rate of 1,2-DCB (because of higher boiling point) facilitated self-organization and ordering of P3HT and promoted finer phase separation. Higher local hole mobility in 1,2-DCB-based blend was attributed to efficient hole transport through the ordered network of P3HT chains. Moreover, higher local illuminated current (dark + photocurrent) in 1,2-DCB-based blend suggested efficient diffusion and dissociation of excitons due to finer phase separation. As a consequence, 1,2-DCB-based devices exhibited higher short circuit current density (J_{sc}), external quantum efficiency and power conversion efficiency in contrast to the CB-based device. It was also observed that the device performance was not limited by light absorption and exciton generation; rather morphology dependent processes subsequent to exciton generation, primarily charge transport to the electrodes, limited device performance. © 2011 Society of Photo-Optical Instrumentation Engineers (SPIE). [DOI: [10.1117/1.3662467](https://doi.org/10.1117/1.3662467)]

Keywords: bulk heterojunction; blend morphology; nanoscale charge transport; hole mobility; scanning probe microscopy; organic solar cell.

Paper 11199R received Jul. 25, 2011; revised manuscript received Oct. 6, 2011; accepted for publication Oct. 28, 2011; published online Nov. 18, 2011.

1 Introduction

Bulk heterojunction (BHJ) solar cells have received considerable attention in recent years due to their strong potential for cost-effective energy conversion and their compatibility with flexible substrates.¹⁻³ The active layer of BHJ solar cells consists of a blend of donor and acceptor materials in a single layer of two conjugated polymers,^{4,5} a combination of conjugated polymer and fullerene,³⁻⁷ or a blend of polymer and inorganic nanocrystals.^{8,9} Under illumination excitons

are generated primarily in the donor material. The excitons diffuse to the donor-acceptor (DA) interfaces where they dissociate, leading to formation of free electrons and holes. Under electric field, dissociated carriers are transported to the respective electrodes where they are collected. Holes flow through the donor material toward the anode and electron flows through the acceptor phase toward the cathode. The nanoscale morphology of the DA blend plays a crucial role in determining the photovoltaic performance of the device.³⁻⁹ A blend of poly(3-hexylthiophene) (P3HT) as donor and phenyl-C₆₁-butyric acid methyl ester (PCBM) as acceptor has been studied extensively as a prototypical BHJ cell, with reported efficiencies up to 5%.^{10,11} In an ideal scenario, phase separation in the blend should lead to the formation of an interpenetrating bicontinuous network of DA materials. The mean domain size of the acceptor PCBM and donor (P3HT) in the blends should lie within the exciton diffusion length (4 to 20 nm)¹²⁻¹⁴ for efficient diffusion of excitons to DA interface. A high degree of DA phase separation with large interfacial area helps exciton dissociation while bicontinuous percolating pathways of interconnecting DA network offer efficient transport of free carriers to the respective electrodes.¹⁵ However, an extremely fine phase separated DA blend is not ideal because it impedes the flow of both excitons and dissociated charge carriers and increases the probability of recombination. Thus, an optimum balance between interpenetrating and interconnecting DA components in the blend is necessary to maximize exciton dissociation and free carrier transport¹⁶ and hence to maximize the cell efficiency.

Various approaches, such as thermal annealing, solvent vapor annealing, mixed solvents, control of spin speed and time, rate of solvent extraction (slow and fast drying), solution precipitation of P3HT nanofibers and nanowires, were used to control and optimize morphology of the blend.¹⁷⁻²⁶ In addition, the morphology of the active layer was also found to be dependent on the donor polymer material which can be controlled using choice of solvent and additives.²⁷⁻²⁹ Among these methods, an effective control of blend morphology can be achieved through the use of appropriate spin-casting solvents for DA components.³⁰ Efforts were made to control blend morphology using a choice of solvent or by using a mixture of two or more solvents, for example toluene, benzene, chlorobenzene, chloroform, xylene, and a mixture of dichlorobenzene and chloroform.²⁴⁻³¹ While previous reports showed the influence of the solvents on blend morphology and device performance, little attention was given to connect the physical properties of the solvents to morphological modifications, resulting in changes in carrier mobility, charge transport, and device efficiency. The physical properties of the solvent such as polarity, viscosity, boiling point, evaporation rate, and density may strongly influence the extent of intermixing and the length scale of phase separation of the blends, and therefore development of such correlation through a combination of nanoscale studies and device measurements would significantly help predictive engineering of the morphologies.

A variety of scanning probe microscopy (SPM)-based techniques such as atomic force microscopy (AFM),³¹ scanning tunneling microscopy,³² electrostatic force microscopy,³³ Kelvin probe force microscopy,^{34,35} conductive atomic force microscopy (C-AFM),^{33,36} and near-field scanning optical microscopy^{37,38} have been used in recent years to study the morphology and nanoscale optoelectronic properties of the blend. Thus, measurement of nanoscale structural, electrical, and optical properties of the active layer with high spatial resolution using SPM-based methods can be used in conjunction with device scale measurements to correlate physical properties of the solvent to blend morphology, nanoscale charge transport processes, and device performance.

This report examines the relationship between the physical properties of the spin-casting solvent, nanoscale morphology, local charge transport, and final device performance of P3HT:PCBM blends spin cast from two halogenated aromatic solvents: chlorobenzene (CB) and 1,2-dichlorobenzene (1,2-DCB) using a combination of nanoscale and macroscale measurements. The role of solvent properties such as boiling point, evaporation rate, solubility, and polarity in controlling the morphology of blends was investigated. Subsequently, the effect of fine (optimal) and coarse morphology on local photocurrent generation and nanoscale charge transport was also studied and correlated to device performance. AFM-based topography and

phase imaging were used to study the surface morphology and to identify DA components with high spatial resolution. Blend morphology was also studied using bright field transmission electron microscopy (TEM) imaging. The local hole current was measured under dark and illumination conditions (532 and 680 nm wavelengths) by injecting holes into the blend using a C-AFM tip and collecting at the bottom ITO electrode. Since the hole transport pathways were through the thickness of the films, C-AFM results were likely to give an indication of the overall nature of the charge transport pathways and organization of DA phases in the bulk of the films. C-AFM-based current-voltage spectroscopy was conducted to estimate and compare local hole mobility of the blends using a space charge limited current equation.³³ Hole transport was specifically discussed because hole mobility is smaller than electron mobility in these blends and limits the final device performance.¹⁴ Finally, the connections between solvent physical properties, blend morphology, charge transport, and device performance were established.

2 Experimental Section

For the deposition of the active blend layer, ITO glass slides were cleaned, dried, and then treated in O₂ plasma for 30 min to remove any organic residue. Poly(3,4-ethylenedioxythiophene):poly(styrenesulfonate) (PEDOT:PSS) was spin-coated onto ITO-glass substrates at 4000 rpm for 30 s and were annealed at 140°C for 20 min. A mixture of regioregular RR-P3HT (10 mg/ml; Rieke Met. Inc) and PCBM (10 mg/ml; Nano-C) in corresponding solvents (CB and 1,2-DCB) were spin-coated onto the PEDOT/PSS layer. The spin-casting process involved two steps: the initial 100 rpm for 20 s followed by 800 rpm for 20 s (continuous process without stops). The same process was used for both CB and 1,2-DCB solvent-based blends. The films (not dry) were left in a Petri dish. Finally, samples were annealed at 140°C for 10 min. The active layer thickness was measured and found to be 100 to 120 nm. Most of the time, the CB film has a slightly higher thickness than the 1,2-DCB film. For device studies, an interfacial layer of Ca was deposited onto the blend film followed by thermal evaporation of about 200-nm thick Al back electrode. The devices were post-annealed at 140°C for 10 min. Complete device fabrication was carried out inside an environmentally controlled glove box. Multiple sets of P3HT:PCBM blend films were prepared using CB and 1,2-DCB solvents and stored in the glove box to avoid exposure to humidity and oxygen.

AFM measurements were conducted using an Agilent 5500 microscope in a hermitically sealed chamber under dry nitrogen atmosphere. Silicon tips (Budget Sensors; nominal resonance frequency ≈ 75 kHz, force constant ≈ 3 N/m; tip radius of ~ 10 nm) were used for conducting topography and phase imaging simultaneously. All the samples were imaged using the same AFM tip. High resolution AFM images were measured using a SuperSharp silicon probe (Nanosensors) with nominal resonance frequency ≈ 190 kHz and tip radius less than 5 nm. Conducting AFM images and location specific current-voltage spectroscopy measurements were performed in contact mode using Pt-Ir coated Si (Budget Sensors; radius ~ 20 nm; force constant of 0.2 N/m; resonance frequency ≈ 14 kHz). A cantilever with small force constant, such as the one used here, permits repeated imaging soft polymer surface without deformation, which is important to ensure reproducible electrical contact between the tip and the sample and also to limit the tip induced amplification of the local current because of hard contact. Further, the measurements were conducted at the lowest set point regimes when the tip softly touches the surface so as to collect the current without damaging the structure. Current images with ~ 20 nm spatial resolution limited by the tip radius were obtained simultaneously with topography images. The conducting probe makes contact with the sample and measures the current as a function of the applied voltage at certain points on the surface producing local $I-V$ plot or produces current maps at a fixed bias at each image pixel. The holes were injected from a conducting Pt/Ir coated AFM tip into P3HT and collected at the grounded ITO electrode. The hole current was measured using an in-built preamplifier with 1 nA/V sensitivity. The images were taken at 0.5 V bias to avoid tip induced local oxidation/reduction. Each of the $I-V$ plots were taken by locating the tip to a new position (fresh area) after every measurement. Photocur-

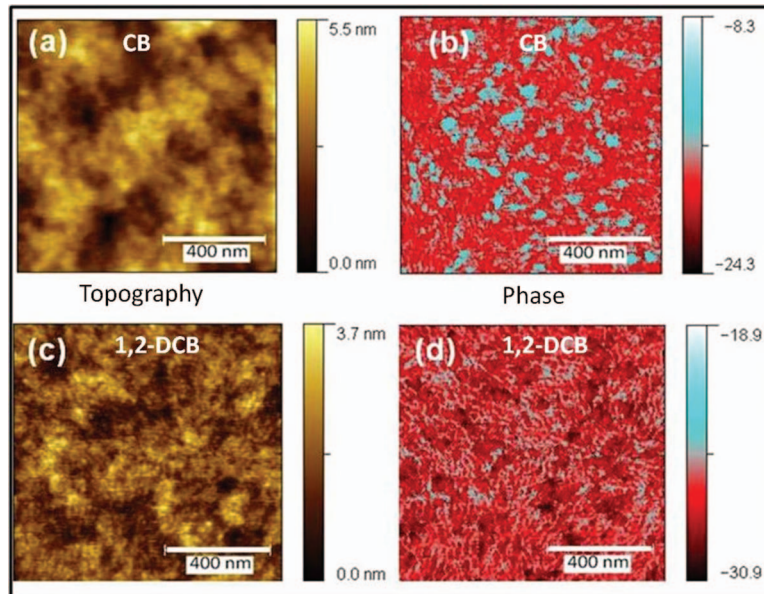


Fig. 1 (a) and (c) Topography images of P3HT:PCBM blended films spin cast from CB and 1,2-DCB solvents, respectively. (b) and (d) show the corresponding phase images identifying the components of the blend mixture. The chain-like self-assembly of P3HT was observed in the 1,2-DCB-based film in contrast to larger and isolated domains in the CB-based blend. The 1,2-DCB-based blend showed finer phase separation than the CB-based blend.

rent measurements were conducted by illuminating a small area on the sample, from the bottom, using 532 nm (green) and 680 nm (red) lasers with photon flux up to $\approx 10^{18}$ photons/s-cm². The intensity of the laser was kept low to avoid local heating of the sample and the tip and the laser spot was carefully focused on the sample at a very small region underneath the tip. Unwanted contribution from thermally generated carriers and local degradation of the film due to heating was thus avoided. For TEM measurements, P3HT:PCBM active layers were floated on deionized water and collected on 200 mesh copper grids. The samples were subsequently dried at room temperature and kept inside a vacuum desiccator overnight to prevent any morphological change due to unwanted thermal annealing.³⁹ Bright field TEM imaging was conducted using a Hitachi H-7000 instrument fitted with LaB6 filament under a slightly defocused condition. Multiple images were acquired at different locations of the film under uniform illumination using a gain-corrected CCD camera. A low accelerating voltage of 100 keV was used to avoid altering the film morphology by electron beam induced damage. Thickness of the blends was measured using a Dektak profilometer as well as by imaging a step created on the film using AFM. UV-Vis absorption spectra of the films on quartz plates were collected using an Agilent 8453 spectrometer. Device $J-V$ and external quantum efficiency (EQE) measurements were conducted by two probe methods using a National Institute of Standards and Technology (NIST) calibrated Newport Solar simulator (AM 1.5 illumination, 100 mW/cm²).

3 Results and Discussion

Figure 1 shows the surface topography [Figs. 1(a) and 1(c)] and phase images [Figs. 1(b) and 1(d)] of P3HT:PCBM blends spin cast from CB and 1,2-DCB solvent, respectively. The topographic (height) images show distributed domains of P3HT and PCBM. A distinct difference in the surface morphology of donor and acceptor components was noticeable among the blends cast from CB and 1,2-DCB which was more evident in the phase images. Self-organization of polymer P3HT chains was observed for a 1,2-DCB-based blend similar to the fiber-like polymer chain reported in literature.³³ Phase imaging was done in net-attractive regime, with

about 50% damping in the amplitude of free cantilever vibration. Softer and elastic regions of the sample dampens AFM cantilever vibrations more than that at harder regions leading to higher phase difference from the reference drive signal.⁴⁰ Thus, it is possible to identify individual components of a heterogeneous mixture from the compositional mapping of the surface provided by the phase images. The brighter regions in phase images (higher phase) correspond to the softer⁴¹ P3HT polymer rich regions. In contrast, darker regions (lower phase) were assigned to harder PCBM rich domains. Moreover, phase images do not have direct one-to-one correlation with topographic (height) images and are more useful to distinguish components of a heterogeneous blend based on the difference in the viscoelastic properties of the individual components. It is also to be noted that the term “phase” corresponds to the donor P3HT and acceptor PCBM rich regions which has no connection with the crystalline and amorphous regions of the materials which are often referred to as phase in other structural measurements. The phase images of CB and 1,2-DCB-based films showed a significant variation in the length scales of DA phase separation. Morphology of the films prepared with a CB solvent showed coarser phase separation with large domains of P3HT (brighter regions) separated by PCBM clusters. The size of P3HT domains and PCBM clusters vary from 30 to 110 nm and 25 to 100 nm, respectively. For statistical validity, several images of different locations along with the representative images (shown in Fig. 1) were analyzed to estimate the sizes; whereas blends cast from 1,2-DCB exhibited a finer phase separation of 10 to 15 nm length scale and an ordered network of P3HT polymer chains.

Further morphological studies were conducted by TEM where an indication of the internal structure of the film can possibly be obtained since electrons are detected after they have traversed through the entire film.^{42,43} Figures 2(a) and 2(b) show representative TEM images of the active layer spin cast with CB and 1,2-DCB solvents, respectively. Due to the difference in density of P3HT (1.1 g/cm³) and PCBM (1.5 g/cm³), TEM can distinguish these two phases with P3HT rich regions appearing brighter (white areas) than the PCBM rich regions (dark areas).⁴⁴ However, it is to be noted that thickness variations in the film can sometimes result in false image contrast and therefore need to be distinguished from density contrast using proper imaging conditions. From the significant variation of a fast Fourier transform pattern and image contrast reversal at under- and over-focused conditions, it was confirmed that the contrast in TEM images was indeed dominated by phase or density contrast and not due to thickness variations. Moreover, AFM measurements revealed that the films are quite uniform and smooth (rms roughness less than 0.9 nm). A coarse morphology with large clusters (about 40 to 100 nm) of P3HT rich regions separated by PCBM rich regions was observed in the CB-based film similar to that observed in AFM images. Self-ordering and chain formation which is usually observed in P3HT was absent in the CB-based film under present processing conditions. However, 1,2-DCB cast blend showed a higher degree of intermixing and finer phase separation of the DA phases than CB cast film. High resolution AFM phase image [Fig. 3(a)] and TEM image [Fig. 3(b)] of 1,2-DCB cast blend showed the finer intermixing of DA components with an ordered network of P3HT chains and matched well with each other. From Figs. 3(a) and 3(b) it was observed that the length of individual P3HT polymer self-assemblies and their diameter varied between 25 and 70 nm and 10 and 20 nm, respectively. The size of the PCBM clusters occupying the space between two P3HT chains varied from 10 to 15 nm. This suggests that two successive polymer chains were separated within the exciton diffusion length (usually 4 to 20 nm)¹² with PCBM nanoclusters embedded in-between. Therefore, in contrast to CB cast blend, 1,2-DCB cast blend showed improved polymer ordering, higher degree of phase separation, and efficient blending of DA phases, which facilitated both exciton dissociation and carrier transport in the active layer.

The physical properties of the solvent, such as boiling point, viscosity, density, and polarity, significantly influence the extent of phase separation.^{24,45,46} Different physical properties of CB and 1,2-DCB are summarized in Table 1. Fullerene is less soluble in CB than in 1,2-DCB,⁴⁷ and larger clusters of PCBM in CB-based films may be a result of poor solubility leading to early precipitation of PCBM during solvent evaporation, especially during the thermal annealing

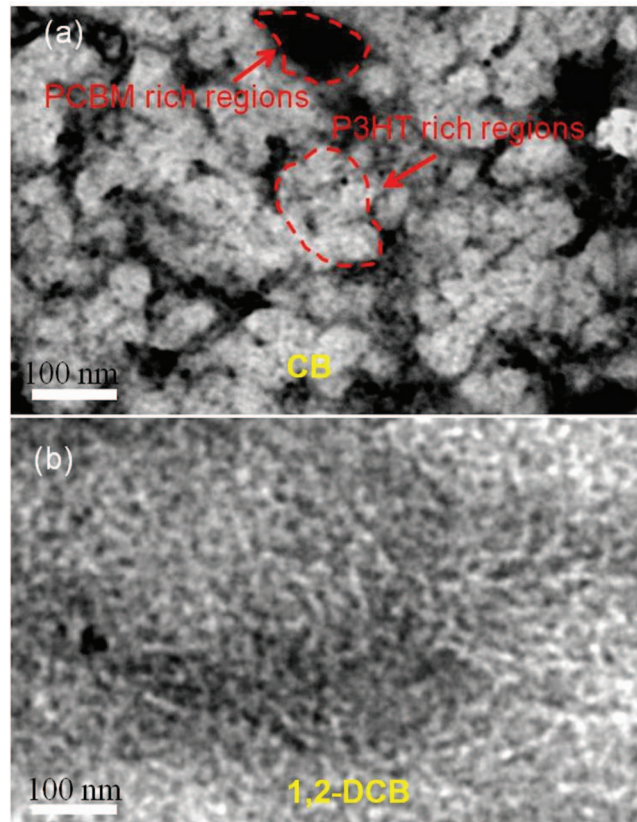


Fig. 2 TEM images of P3HT:PCBM blends prepared with (a) CB and (b) 1,2-DCB solvents. (a) shows a coarse morphology of CB cast active layer with P3HT rich (brighter) and PCBM rich (darker) regions isolated in large domains. Two domains of P3HT and PCBM rich regions are marked. (b) 1,2-DCB cast film shows a uniformly distributed and ordered P3HT:PCBM blend with a higher degree of phase separation as compared to the CB-based blend. Fiber-like P3HT chains were observed throughout the film.

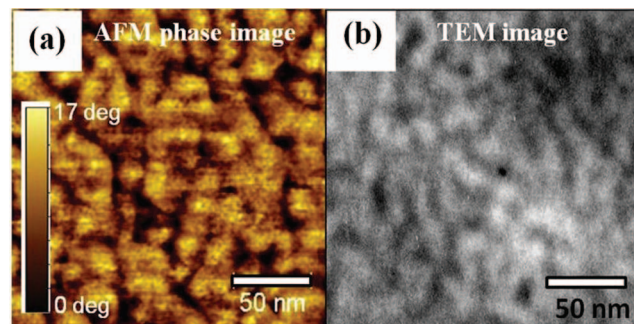


Fig. 3 High resolution (a) AFM phase and (b) TEM (phase contrast) images of P3HT:PCBM blend prepared with 1,2-DCB solvent. A strong correlation between the AFM and TEM images was observed. A self-ordered and interpenetrating network of P3HT and PCBM was observed, which led to an optimum phase separation of 10 to 15 nm. The feature size in the AFM phase images was slightly larger owing to finite probe size (≈ 5 nm diameter).

Table 1 Physical properties of CB and 1,2-DCB solvents.

Material (solvent)	Boiling point	Dipole moment	Viscosity (cP)	Molecular weight (g)	Density (g/cc)
Chlorobenzene (CB)	131°C	1.5	0.80	112.56	1.11
	180.5°C	2.27	1.32	147.0	1.31

process when the residual solvent evaporates quickly from the blend. Moreover, relatively poor solubility of P3HT in CB may have resulted in incommensurate self-organization of polymer chains. Poor solubility of both P3HT and PCBM has been attributed to the lower polarity of CB. On the other hand, higher solubility of both P3HT and PCBM due to higher polarity of 1,2-DCB solvent may be responsible for highly organized self-assembly of P3HT and finer phase separation.⁴⁸ Therefore, improved solubility of DA components may have resulted in effective interpenetration of P3HT and PCBM networks leading to finer phase separation in 1,2-DCB cast blend.

Several recent reports suggested that a higher solubility of DA components leads to lower surface roughness of polymer blends and enhanced device efficiency.^{6,10} A comparative study with CB- and toluene-based blends showed that the CB-based blend yields a smoother film due to higher solubility of PCBM in CB. Higher solubility of CB also led to an increased intermixing of the DA phases, resulting in improved charge collection and higher device efficiency.⁶ On the contrary, other reports⁴⁹ stated that rough surface of blend film is a signature of higher efficiency. It was argued that the rougher surface increased charge collection by increasing the contact area between blend and metal cathode at the interface and also increased light absorption by improving internal reflection. However, an increase in efficiency was not directly attributed to increased roughness, but to improved ordering of P3HT chains and optimal DA phase separation in both lateral and vertical directions. Our studies showed an interesting correlation between surface root-mean-square roughness (R_{rms}) and solubility of the DA components in the spin casting solvent. R_{rms} of CB- and 1,2-DCB-based P3HT:PCBM blends was 0.89 and 0.55 nm, respectively, as measured by AFM. Results showed that a smoother surface was obtained for blends prepared with a solvent of higher solubility (1,2-DCB). A smoother surface is likely to improve the adhesion between electron transport layer (Ca) and the blend film, thereby reducing recombination of charge carriers at the interface and increasing device efficiency.⁶ Moreover, slow solvent evaporation may also lead to a smoother film surface and improved vertical phase separation, resulting in efficient percolation pathways and enhanced charge collection.⁵⁰ Furthermore, it has been reported that fast solvent removal leads to the reduction of P3HT crystallinity and also increases the interlayer distance of the polymer in the blend film.⁴⁸ In addition, rapid evaporation of solvent during thermal annealing induces Marangoni instability in the bulk of the film which roughens the surface of the film leading to insufficient phase separation.⁴⁸ Therefore, high surface roughness ($R_{\text{rms}} = 0.89$ nm) and coarse phase separation of a CB cast film was also attributed to the rapid solvent evaporation because of its low boiling point (131°C). On the other hand, a higher boiling point of 1,2-DCB (181°C) and correspondingly its slower evaporation rate resulted in a smoother film ($R_{\text{rms}} = 0.55$ nm) and finer phase separation. Further, a high viscosity of 1,2-DCB (see Table 1) may also have promoted efficient phase separation during spin coating, as observed by Arias et al.⁵⁰ Therefore, higher solubility, boiling point (low rate of evaporation), and viscosity are desirable properties of a spin-casting solvent which results in a smoother surface and facilitates finer phase separation in the blend.

The effect of nanoscale phase separation on photocurrent generation and nanoscale charge transport is described here. A schematic of nanoscale charge (here hole) injection using C-AFM is shown in Fig. 4(a) and the corresponding energy band diagram is shown in Fig. 4(b). Holes were injected from the Pt-coated tip into the blend and collected at the ITO electrode, meaning that the holes pass through the entire thickness of the active layer before being collected at the anode. Therefore, the information obtained from C-AFM measurements may be considered to reflect the overall electrical quality of the active layer, not just the surface. Some of the previous

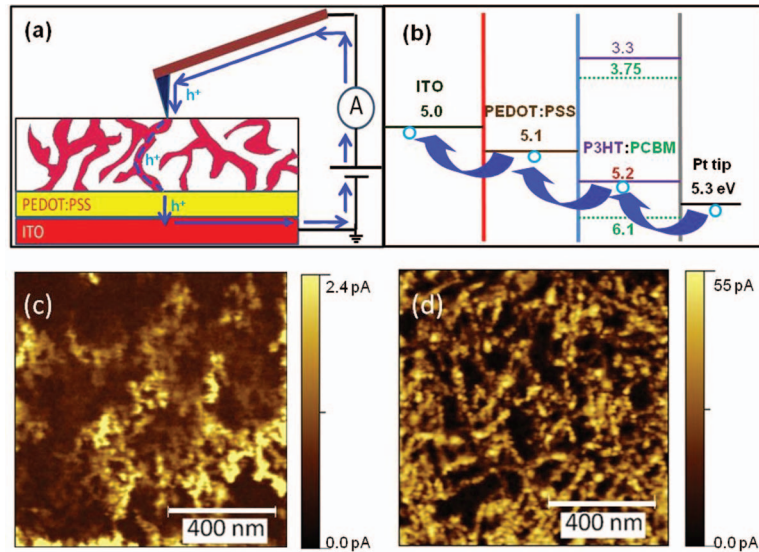


Fig. 4 (a) Schematic of C-AFM set-up. (b) Band diagram showing the injection of holes from the tip to the back contact ITO. The work function of the tip is suitable for detecting hole current through the film. C-AFM images showing the hole current distribution in the P3HT: PCBM blend films spin cast with (c) CB and (d) 1,2-DCB solvents, respectively. The local charge (hole) transport through interconnecting P3HT polymer chains (brighter regions, mainly in 1,2-DCB-based blend) can be directly observed at nanoscale resolution.

studies have also used Mg and Au (Refs. 36 and 51) coated tips to probe electron current in a similar structure. However, hole current measurements were specifically conducted here since lower hole mobility usually determines carrier transport in polymer solar cells and limits final device performance.³⁶ The C-AFM images of the blends prepared with CB and 1,2-DCB solvents are shown in Figs. 4(c) and 4(d), respectively. Brighter areas in the images are high hole current regions corresponding to P3HT rich areas and darker areas are low hole current regions corresponding to PCBM rich areas.³⁶ Blends prepared with CB showed discontinuous regions of P3HT and PCBM isolated at longer length scales (25 to 100 nm). On the other hand, the 1,2-DCB-based film showed a network of cross-linked P3HT polymer chains extended throughout the surface. The maximum current corresponding to P3HT rich areas in 1,2-DCB cast films was ≈ 55 pA, whereas maximum current in the CB-based film was ≈ 3 pA. Moreover, the C-AFM images taken with zero sample bias ($V = 0$) showed no contrast, indicating a negligible effect of topography on current images. Also, the C-AFM images could not be acquired under sample bias with negative polarity (current was well below 2 pA, noise floor of the measurement setup), because the Pt tip is not suitable for collection or injection of electrons due to a large mismatch of Fermi energy with the lowest unoccupied molecular orbital of PCBM.³⁶

Local dark $I-V$ spectroscopy (where I is the hole current) was performed at different P3HT rich locations on the surface and the averaged $I-V$ plot was used for the estimation of hole mobility. The dark $I-V$ plots conducted on films spin cast with CB and 1,2-DCB are shown in Fig. 5. A nonlinear increase in hole current at positive and negative bias polarities suggested a non-Ohmic contact between the sample and the tip.^{52,53} The hole injection barrier in the forward bias region (~ 50 mV) was significantly smaller than the reverse bias region (~ 0.8 V). This was attributed to a lower potential barrier between the tip and P3HT compared to ITO and electrode as shown in the band diagram.⁵² The hole transport showed a quadratic dependence with bias for both the samples following the space-charge limited current (SCLC) model:^{36,53}

$$J = \frac{9}{8} \epsilon \epsilon_0 \mu \frac{V^2}{L^3}, \quad (1)$$

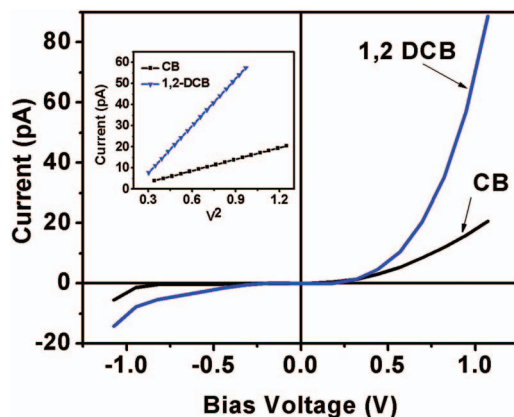


Fig. 5 Local dark I - V plots of the blends spin cast with CB and 1,2-DCB solvent. Inset shows local dark I - V plots from C-AFM measurements fitted using the SCLC equation for calculation of hole mobility. Hole mobility can be estimated from the slopes of the fitted curves. From the curves it is seen that the 1,2-DCB-based blend has higher hole current and mobility compared to the CB cast blend.

where ε is the dielectric constant of the polymer, ε_0 is the vacuum permittivity, μ is the hole mobility, V is the applied voltage, and L is the film thickness. A nominal tip radius of 20 nm was used to estimate the current density. Using the SCLC Eq. (1), the field independent hole mobility was calculated by fitting the quadratic region of the dark current under forward bias^{53,54} and is shown in the inset of Fig. 5. The hole mobility of CB and 1,2-DCB blend was 4.64×10^{-3} and $14.0 \times 10^{-3} \text{ cm}^2 \text{ V}^{-1} \text{ s}^{-1}$, respectively. It has been reported that hole mobility measurements by C-AFM yields values an order of magnitude greater than bulk I - V measurements and most reports apply appropriate corrections to calculate accurate values.⁵⁴ In this study, instead of calculating the exact values of the hole mobility, the goal was to compare the hole mobility of the two films estimated from the SCLC equation. The increase in hole mobility in 1,2-DCB cast blend may be attributed primarily to the ordering of the P3HT chains, allowing an efficient pathway for hole transport, thereby improving hole collection.

UV-Vis absorption spectra of the blend films are shown in Fig. 6, which indicates higher absorption in the CB film in the visible region (400 to 550 nm) than the 1,2-DCB-based film. Thus, the CB cast blend showed better light harvesting capability than the 1,2-DCB cast blend, resulting in an increased exciton generation in the device. The absorption peaks of 1,2-DCB cast film were redshifted with respect to that of the CB cast film, indicating a significant increase in ordering, interchain interaction, and crystallinity²⁴ of P3HT polymer phase in the 1,2-DCB cast films as compared to the CB-based film, which was supported by AFM (Fig. 1) and TEM data (Fig. 2). Also, the prominent shoulder at ~ 600 nm observed in 1,2-DCB blend was also indicative of stronger interplane interaction due to enhanced self-organization of P3HT.⁴²

Figure 7 shows a local current-voltage response of blends under 532 nm laser illumination. Measurements were performed at low and high photon absorption regions of P3HT using red (low absorption at 680 nm, not shown here) and green laser (high absorption at 532 nm). Inset shows the I - V plots of 1,2-DCB blend acquired in dark and using red and green laser source. The conductive AFM tip was carefully positioned at P3HT rich areas. The measurements were performed at multiple locations and the standard deviation was within 10% for a given film. A distinct kink of S-shape was observed in the I - V response of 1,2-DCB cast film under green illumination in the forward bias which was not observed in the dark I - V or in I - V response under red illumination (inset) for a CB cast film. Stronger absorbance of green light compared to that of red in P3HT and optimum phase separation in a 1,2-DCB film resulted in higher density of photogenerated holes, suggesting a role of high hole density in the formation of the kink. It is important to note that the present AFM-based hole-only I - V spectroscopy is different from

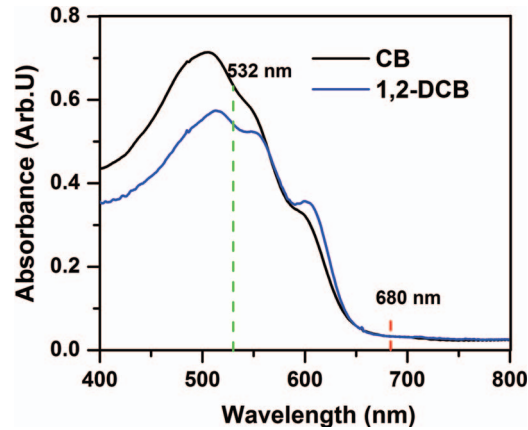


Fig. 6 UV-Vis absorption spectra of the P3HT:PCBM blend films spin cast with CB and 1,2-DCB solvents on quartz plates. Absorbance peaks of 1,2-DCB cast blend shows a considerable redshift in the 400 to 550 nm range relative to CB cast blend. The two vertical lines show the relative absorbance of the blends at 532 and 680 nm wavelength regions.

typical device I - V measurements, where both electrons and holes are extracted. Therefore, direct comparison of present results with device-based measurements⁶ requires careful consideration on unbalanced carrier extraction⁵⁴ with excessive electron accumulation in the active layer. The excess photogenerated holes in a 1,2-DCB cast film may be accumulated at the P3HT-PEDOT:PSS interface, which may result in the voltage dependent local current measurement and the kink in the I - V curve under green illumination.⁵⁵⁻⁵⁷ A similar S-shaped I - V curve was reported for P3HT:PCBM-based BHJ devices under illumination, and not in the dark.⁵⁸ Moreover, an increase in local hole current under illumination was observed at higher positive (forward) bias, whereas short circuit current I_{sc} (at $V = 0$) was ≈ 0.5 to 1 pA, which is close to the noise floor of the measurement setup. The absence of I_{sc} in local I - V plots can be attributed to an insufficient built-in electric field (~ 0.2 eV) between the Pt tip (work function $\Phi = 5.3$ eV) and the ITO electrode ($\Phi = 5.1$ eV), resulting in poor collection of photogenerated holes by point-contact of the AFM tip at zero external bias. A similar low photoresponse was reported by Douh  ret et al.⁵² using Pt coated tips.

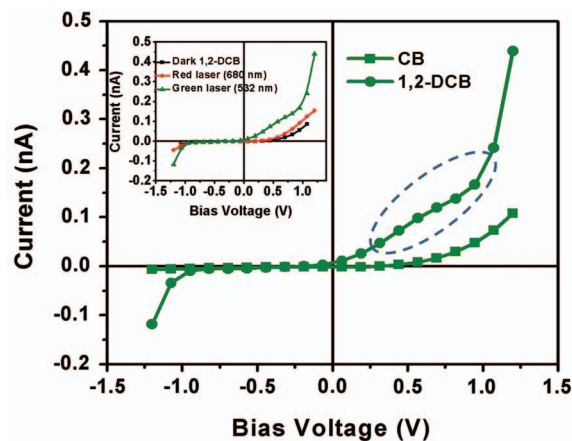


Fig. 7 Local illuminated I - V plots of CB- and 1,2-DCB-based films under green light illumination. The dotted line shows the anomalous S-shaped kink in the I - V curve of the 1,2-DCB spin cast film. Inset shows local I - V curves of the 1,2-DCB film taken in the dark and under 680 and 532 nm wavelength illumination.

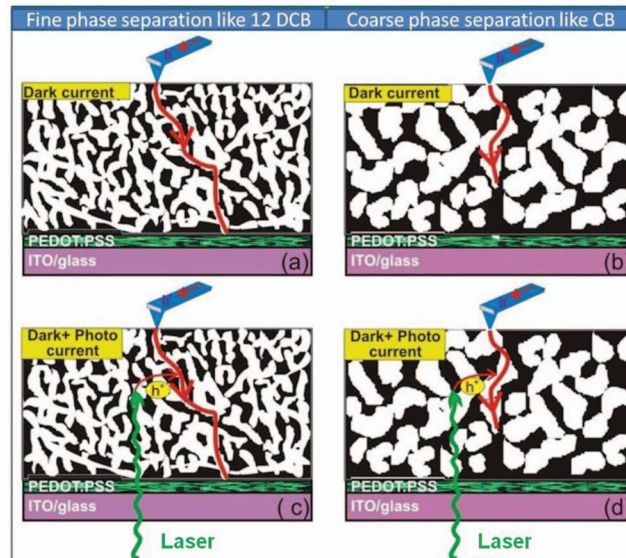


Fig. 8 Proposed model showing a distinct difference in the morphology, phase separation, and its effect on the efficiency of charge transport in P3HT:PCBM blends with (a) and (c) fine and (b) and (d) coarse phase separation. Here, dark regions represent the PCBM phase and white regions represent the P3HT phase. The path of the hole current from the AFM tip through the P3HT into the ITO electrode is shown. A P3HT network with fine phase separation and ordered morphology (such as 1,2-DCB cast blend) results in efficient transport of injected holes (a) and photogenerated holes (c), similar to the 1,2-DCB-based blend. Coarse phase separated blend (such as CB cast blend) with discontinuous or isolated DA domains results in the loss of injected (b) and photogenerated holes (d).

A proposed conceptual model based on the information obtained from local charge transport and morphology studies, distinguishing a fine (similar to 1,2-DCB-based blends) and coarse (similar to CB-based blend) phase separated active layer is shown in Fig. 8. Here, dark regions represent the PCBM phase and white regions represent the P3HT phase. The origin of the dark current is primarily the holes injected by an AFM tip into the DA blend, which were collected at the ITO substrate. A complete path of dark hole current from AFM tip through the ordered network of P3HT phase to the ITO electrode is shown in Fig. 8(a). Availability of complete pathways of hole transport might have resulted in higher local dark hole current and hole mobility for 1,2-DCB-based blend. On the other hand, an interrupted pathway of hole current in CB cast blend is shown in Fig. 8(b). Smaller dark current and low hole mobility of CB cast blend suggested increased recombination of injected holes due to the absence of such ordered pathways. Figures 8(c) and 8(d) show the effect of fine and coarse phase separated morphology on the illuminated current. Photogenerated holes (after exciton dissociation) add up to the injected dark holes to give the total hole current under illumination.⁴⁹ Thus, illuminated current is a measure of the efficiency of exciton generation, diffusion, and dissociation controlled by the interpenetrating fine phase separated network.⁵³ Phase separation in 1,2-DCB-based blend (10 to 15 nm) is of the same order of exciton diffusion length (~ 4 to 20 nm);¹² such fine phase separation provides an increased DA interfacial area, which facilitates efficient exciton dissociation and reduces the probability for geminate exciton recombination.⁵⁹ This explains the higher illuminated current in the 1,2-DCB-based blend. In the case of a CB-based film, the donor and acceptor domains are distributed in large isolated patches. The phase separation length varied from 25 to 100 nm in the case of CB and is greater than the exciton diffusion length. This explains the low illuminated current in CB as compared to the 1,2-DCB blend. Thus, the proposed model and experimental evidence suggest that the morphology of the 1,2-DCB blend

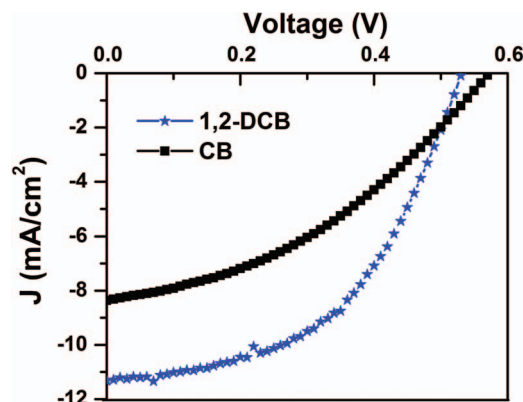


Fig. 9 Device J - V plots of the P3HT:PCBM blends prepared with CB and 1,2-DCB solvents. Higher PCE was obtained for the blend prepared with 1,2-DCB solvent.

was optimal for efficient exciton diffusion, dissociation through fine phase separated ordered DA network, and also facilitated efficient carrier separation, transport, and charge collection through the ordered DA network as opposed to the CB-based blend.

Finally, the performance of the devices fabricated using CB and 1,2-DCB cast active layers were compared using illuminated J - V plots (Fig. 9). Power conversion efficiency (PCE), open circuit voltage (V_{oc}), short circuit current density (J_{sc}), and fill factor (FF) of the two cells are summarized in Table 2. The FF and PCE of the 1,2-DCB-based cell were 50% and 3.1%, respectively, whereas FF and PCE of the CB-based cell were 38% and 1.9%, respectively. There was a 60% increase in the PCE of the 1,2-DCB-based cell compared to that of the CB-based cell which was quite significant on the basis of the distinct difference in morphology of the two blends. The EQE of the CB- and 1,2-DCB-based cells at 532 nm were 55.3% and 72.9%, respectively (see Fig. 10). As predicted from the optimum nanoscale morphology, the 1,2-DCB-based device gave the maximum PCE and EQE.

Though the light absorption and exciton generation efficiency of the 1,2-DCB cast film was significantly lower than the CB cast film, the PCE of the 1,2-DCB-based BHJ cell was found to be higher than the CB-based device. This suggests that the ability of the blends (primarily P3HT) to efficiently absorb light and generate excitons was not the only deciding factor for better photovoltaic performance of the cells and does not necessarily lead to higher efficiency. Instead, the final device performance was strongly determined by the processes subsequent to charge generation: exciton dissociation, carrier separation, transport, and collection at the electrodes which are, in turn, strongly dependent on blend morphology. One of the possibilities may be that the exciton dissociation and free charge transport through the 1,2-DCB cast film was facilitated due to the more evolved morphology and ordered network of DA phases. Whereas, in spite of the efficient generation of excitons in a CB cast film, the majority of the excitons may have remained undissociated and undergone geminate recombination due to the unavailability of DA interfaces as a result of coarse phase separation. Another possibility might be that the free carriers (after exciton dissociation) were not able to transport efficiently to the electrodes due to the lack of ordered DA pathways.

Table 2 Parameters from bulk J - V measurements.

	CB	1,2-DCB
J_{sc} (mA/cm ²)	8.4	11.3
V_{oc} (V)	0.58	0.54
FF (%)	38	50
Efficiency (%)	1.9	3.1

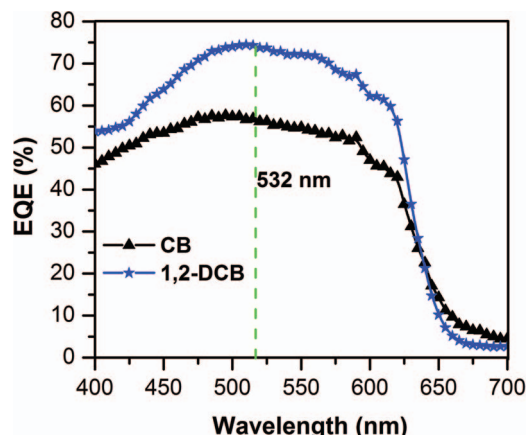


Fig. 10 EQE versus wavelength plots of CB and 1,2-DCB cast devices. The EQE of CB- and 1,2-DCB-based cells at 532 nm were 55.3% and 72.9%, respectively. The 1,2-DCB cast device showed a higher EQE than the CB cast device.

Thus, information obtained through both structural and electrical measurements at nanoscale and device level suggested that the higher boiling point and solvating power of 1,2-DCB led to finer phase separation of DA components and induced ordering in the P3HT phase during film formation, which led to improved exciton dissociation, charge transport, and collection, and finally resulted in a comparative enhancement of device performance. The correlation between the physical properties of spin-casting solvent, morphology, charge transport, and device efficiency was established.

4 Conclusions

A combination of high spatial resolution scanning probe-based measurements, TEM imaging, and device scale measurements was used to investigate the effect of the spin-casting solvents in manipulating the nanoscale morphology of P3HT:PCBM blends and to correlate local charge transport processes with device performance. Results indicate that higher solubility of P3HT and PCBM in 1,2-DCB and a slower evaporation rate (higher boiling point) of 1,2-DCB allowed efficient phase separation of the blend, promoted ordering in P3HT, and resulted in a smoother blend surface. The 1,2-DCB-based blend showed a finer phase separation of ~ 10 to 15 nm, while the blend spin cast with CB exhibited a coarse phase separation of ~ 25 to 100 nm, suggesting higher exciton diffusion and dissociation probability for the 1,2-DCB blend. The P3HT chain alignment and nanoscale self-assembly were more evolved in the 1,2-DCB-based blend which further facilitated efficient charge transport and collection, as indicated by the highest hole mobility in these blends. Therefore, a nanomorphology with finer phase separation and efficient hole transport pathways resulted in a higher power conversion efficiency (3.1%) for the 1,2-DCB-based solar cell. It was also observed that the device performance was not limited by photon absorption and exciton generation; rather the morphology dependent processes subsequent to carrier generation, primarily carrier transport, were limiting the device performance. Thus, the physical property of the spin-casting solvent, blend morphology, and nanoscale electrical properties of the DA blend were correlated with the energy conversion efficiency of the final devices.

Acknowledgments

This research was supported by the National Science Foundation (CMMI-1063263, DMR-0960131, DMR-0923115, and ECCS-0950731), South Dakota EPSCOR (Grant No. 091948), NASA EPSCoR (NNX09AP67A), ACS Petroleum Research Funds DNI (48733DNI10),

US-Israel Binational Science Foundation (2008265), and US-Egypt Joint Science & Technology Funds (913).

References

1. G. Li, V. Shrotriya, J. Huang, Y. Yao, T. Moriarty, K. Emery, and Y. Yang, "High-efficiency solution processable polymer photovoltaic cells by self-organization of polymer blends," *Nature Mater.* **4**, 864–868 (2005).
2. C. J. Brabec, N. S. Sariciftci, and J. C. Hummelen, "Plastic solar cells," *Adv. Funct. Mater.* **11**, 15–26 (2001).
3. G. Yu, J. Gao, J. C. Hummelen, F. Wudl, and A. J. Heeger, "Polymer photovoltaic cells: Enhanced efficiencies via a network of internal donor-acceptor heterojunctions," *Science* **270**, 1789–1791 (1995).
4. G. Yu and A. J. Heeger, "Charge separation and photovoltaic conversion in polymer composites with internal donor/acceptor heterojunctions," *J. Appl. Phys.* **78**, 4510–4515 (1995).
5. J. J. M. Halls, C. A. Walsh, N. C. Greenham, E. A. Marseglia, R. H. Friend, S. C. Moratti, and A. B. Holmes, "Efficient photodiodes from interpenetrating polymer networks," *Nature* **376**, 498–500 (1995).
6. S. E. Shaheen, C. J. Brabec, N. S. Sariciftci, F. Padinger, T. Fromherz, and J. C. Hummelen, "2.5% efficient organic plastic solar cells," *Appl. Phys. Lett.* **78**, 841–843 (2001).
7. M. Siddiki, J. Li, D. Galipeau, and Q. Qiao, "A review on polymer multijunction solar cell," *Energy Environ. Sci.* **3**, 867–883 (2010).
8. S. N. Dayal, D. C. Kopidakis, D. S. G. Olson, and G. Rumbles, "Photovoltaic devices with a low band gap polymer and CdSe nanostructures exceeding 3% efficiency," *Nano Lett.* **10**, 239–242 (2010).
9. Q. Qiao and J. T. McLeskey, "Water-soluble polythiophene/nanocrystalline TiO₂ solar cells," *Appl. Phys. Lett.* **86**, 153501 (2005).
10. W. L. Ma, C. Y. Yang, X. Gong, K. Lee, and A. J. Heeger, "Thermal stable, efficient polymer solar cells with nanoscale controlled of the interpenetrating network morphology," *Adv. Funct. Mater.* **15**, 1617–1622 (2005).
11. J. Y. Kim, K. Lee, N. E. Coates, D. Moses, T. Q. Nguyen, M. Dante, and A. J. Heeger, "Efficient tandem polymer solar cells fabricated by all-solution processing," *Science* **317**, 222–225 (2007).
12. P. Peumans, A. Yakimov, and S. R. Forrest, "Small molecular weight organic thin-film photodetectors and solar cells," *J. Appl. Phys.* **93**, 3693–3723 (2003).
13. D. E. Markov, E. Amsterdam, P. W. M. Blom, A. B. Sieval, and J. C. Hummelen, "Accurate measurement of the exciton diffusion length in a conjugated polymer using a heterostructure with a side-chain cross-linked fullerene layer," *J. Phys. Chem. A* **109**, 5266–5274 (2005).
14. Y. Terao, H. Sasabe, and C. Adachi, "Correlation of hole mobility, exciton diffusion length, and solar cell characteristics in phthalocyanine/fullerene organic solar cells," *Appl. Phys. Lett.* **90**, 103515 (2007).
15. H. Xin, O. G. Reid, G. Ren, F. S. Kim, D. S. Ginger, and S. A. Jenekhe, "Polymer nanowire/fullerene bulk heterojunction solar cells: How nanostructures determines photovoltaic properties," *ACS Nano* **4**, 1861–1872 (2010).
16. C. Deibel and V. Dyakonov, "Polymer–fullerene bulk heterojunction solar cells," *Rep. Prog. Phys.* **73**, 096401 (2010).
17. Y. Xie, Y. Li, L. Xiao, Q. Qiao, R. Dhakal, Z. Zhang, Q. Gong, D. Galipeau, and X. Yan, "Femtosecond time-resolved fluorescence study of P3HT/PCBM blend films," *J. Phys. Chem. C* **114**, 14590–14600 (2010).
18. V. D. Mihailetschi, H. Xie, B. D. Boer, L. M. Popescu, J. C. Hummelen, P. W. M. Blom, and L. J. A. Koster, "Origin of the enhanced performance in poly(3-hexylthiophene): 6,6-phenyl

- C₆₁-butyric acid methyl ester solar cells upon slow drying of the active layer," *Appl. Phys. Lett.* **89**, 012107 (2006).
19. D. Chirvase, J. Parisi, J. C. Hummelen, and V. Dyakonov, "Influence of nanomorphology on the photovoltaic action of polymer-fullerene composites," *Nanotechnology* **15**, 1317–1323 (2004).
 20. H. Hoppe and N. S. Sariciftci, "Morphology of polymer/fullerene bulk heterojunction solar cells," *J. Mater. Chem.* **16**, 45–61 (2006).
 21. Y. Zhao, Z. Xie, Y. Qu, Y. Geng, and L. Wang, "Solvent-vapor treatment induced performance enhancement of poly(3-hexylthiophene):methanofullerene bulk-heterojunction photovoltaic cells," *Appl. Phys. Lett.* **90**, 043504 (2007).
 22. X. Yang, J. Loos, S. C. Veenstra, W. J. H. Verhees, M. M. Wienk, J. M. Kroon, M. A. J. Michels, and R. A. J. Janssen, "Nanoscale morphology of high-performance polymer solar cell," *Nano Lett.* **5**, 579–583 (2005).
 23. M. N. Yusli, T. W. Yun, and K. Sulaiman, "Solvent effect on the thin film formation of polymeric solar cells," *Mater. Lett.* **63**, 2691–2694 (2009).
 24. K. Kawano, J. Sakai, M. Yahiroa, and C. Adachi, "Effect of solvent on fabrication of active layers in organic solar cells based on poly (3-hexylthiophene) and fullerene derivatives," *Sol. Energy Mater. Sol. Cells* **93**, 514–518 (2009).
 25. D. M. DeLongchamp, B. M. Vogel, Y. Jung, M. C. Gurau, C. A. Richter, O. A. Kirillov, J. Obrzut, D. A. Fischer, S. Sambasivan, L. J. Richter, and E. K. Lin, "Variations in semiconducting polymer microstructure and hole mobility with spin-coating," *Chem. Mater.* **17**, 5610–5612 (2005).
 26. Y. Kim, S. A. Choulis, J. Nelson, D. D. C. Bradley, S. Cook, and J. R. Durrant, "Device annealing effect in organic solar cells with blends of regioregular poly(3-hexylthiophene) and soluble fullerene," *Appl. Phys. Lett.* **86**, 063502 (2005).
 27. J. Subbiah, D. Y. Kim, M. Hartel, and F. So, "MoO₃/poly (9,9-dioctylfluorene-co-N-[4-(3-methylpropyl)]-diphenylamine) double-interlayer effect on polymer solar cells," *Appl. Phys. Lett.* **96**, 063303 (2010).
 28. C. M. Amb, S. Chen, K. R. Graham, J. Subbiah, C. E. Small, F. So, and J. R. Reynolds, "Dithienogermole as a fused electron donor in bulk heterojunction, solar cells," *J. Am. Chem. Soc.* **133**, 10062–10065 (2011).
 29. J. Subbiah, K. R. Choudhury, S. Ellinger, J. R. Reynolds, and F. So, "Color tunable π -conjugated polymers for solar-cell applications: Engineering of bandgap, interface, and charge transport properties," *IEEE J. Sel. Top. Quantum Electron.* **16**, 1792–1800 (2010).
 30. Y. Xie, P. Dutta, D. Cengher, V. Bommisetty, J. Li, D. Galipeau, and Q. Qiao, "Solvent effect on the morphology of P3HT/PCBM films," *Proc. SPIE* **7416**, 74161Q (2009).
 31. A. Douhéret, S. Swinnen, I. Bertho, J. D'Haen Haeldermans, M. D'Olieslaeger, D. Vanderzande, and J. V. Manca, "High-resolution morphological and electrical characterisation of organic bulk heterojunction solar cells by scanning probe microscopy," *Prog. Photo-voltaics* **15**, 713–726 (2007).
 32. K. Maturova, R. A. J. Janssen, and M. Kemerink, "Connecting scanning tunneling spectroscopy to device performance for polymer:fullerene organic solar cells," *ACS Nano* **4**, 1385–1392 (2010).
 33. L. S. C. Pingree, O. G. Reid, and D. S. Ginger, "Electrical scanning probe microscopy on active organic electronic devices," *Adv. Mater.* **21**, 19–28 (2009).
 34. H. Hoppe, T. Glatzel, M. Niggemann, A. Hinsch, M. Lux-Steiner, and N. S. Sariciftci, "Kelvin probe force microscopy study on conjugated polymer/fullerene bulk heterojunction organic solar cells," *Nano Lett.* **5**, 269–274 (2005).
 35. K. Maturová, M. Kemerink, M. M. Wienk, S. H. Charrier, and R. A. J. Janssen, "Scanning Kelvin probe microscopy on bulk heterojunction polymer blend," *Adv. Funct. Mater.* **19**, 1379–1386 (2009).

36. M. Dante, J. Peet, and T. Q. Nguyen, "Nanoscale charge transport and internal structures of bulk heterojunction conjugated polymer/fullerene solar cells by scanning probe microscopy," *J. Phys. Chem. C* **112**, 7241–7249 (2008).
37. X. Wang, D. Zhang, K. Braun, H. Egelhaaf, C. J. Brabec, and A. J. Meixner, "High-resolution spectroscopic mapping of the chemical contrast from nanometer domains in P3HT:PCBM organic blend films for solar-cell applications," *Adv. Funct. Mater.* **20**, 492–499 (2010).
38. C. R. McNeill, H. Frohne, J. L. Holdsworth, J. E. Furst, B. V. King, and P. C. Dastoor, "Direct photocurrent mapping of organic solar cells using a near-field scanning optical microscope," *Nano Lett.* **4**, 219–223 (2004).
39. L. F. Drummy, R. J. Davis, D. L. Moore, M. Durstock, R. A. Vaia, and J. W. P. Hsu, "Molecular-scale and nanoscale morphology of P3HT:PCBM bulk heterojunctions: Energy-filtered TEM and low-dose HREM," *Chem. Mater.* **23**, 907–912 (2011).
40. J. P. Cleveland, B. Anczykowski, A. E. Schmid, and V. B. Elings, "Energy dissipation in tapping-mode atomic force microscopy," *Appl. Phys. Lett.* **72**, 2613–2615 (1998).
41. E. Thormann, T. Pettersson, J. Kettle, and P. M. Claesson, "Probing material properties of polymeric surface layers with tapping mode AFM: Which cantilever spring constant, tapping amplitude and amplitude setpoint gives good image contrast and minimal surface damage?," *Ultramicroscopy* **110**, 313–319 (2010).
42. Y. Yao, J. Hou, Z. Xu, G. Li, and Y. Yang, "Effects of solvent mixtures on the nanoscale phase separation in polymer solar cells," *Adv. Mater.* **18**, 1783–1789 (2008).
43. T. J. Savenije, J. E. Kroeze, X. Yang, and J. Loos, "The effect of thermal treatment on the morphology and charge carrier dynamics in polythiophene-fullerene bulk heterojunction," *Adv. Funct. Mater.* **15**, 1260–1266 (2005).
44. X. Yang and J. Loos, "Toward high-performance polymer solar cells: The importance of morphology control," *Macromolecules* **40**, 1353–1362 (2007).
45. L. M. Chen, Z. Hong, G. Li, and Y. Yang, "Multi-source/component spray coating for polymer solar cells," *Adv. Mater.* **21**, 1434–1449 (2009).
46. Y. Yao, C. Shi, G. Li, V. Shrotriya, Q. Pei, and Y. Yang, "Modeling optical effects and thickness dependent current in polymer bulk-heterojunction solar cells," *Appl. Phys. Lett.* **89**, 153507 (2006).
47. R. S. Ruoff, D. S. Tse, R. Malhotra, and D. C. Lorents, "Solubility of C60 in a variety of solvents," *J. Phys. Chem.* **97**, 3379–3383 (1993).
48. K. E. Strawhecker and S. K. Kumar, "The critical role of solvent evaporation on the roughness of spin-cast polymer films," *Macromolecules* **34**, 4669–4672 (2001).
49. G. Li, V. Shrotriya, Y. Yao, and Y. Yang, "Investigation of annealing effects and film thickness dependence of polymer solar cells based on poly(3-hexylthiophene)," *J. Appl. Phys.* **98**, 043704 (2005).
50. A. C. Arias, "Vertically segregated polymer blends: Their use in organic electronics," *J. Macromol. Sci., Polym. Rev.* **46**, 103–125 (2006).
51. L. S. C. Pingree, O. G. Reid, and D. S. Ginger, "Imaging the evolution of nanoscale photocurrent collection and transport networks during annealing of polythiophene/fullerene solar cells," *Nano Lett.* **9**, 2946–2952 (2009).
52. O. Douhéret, L. Lutsen, A. Swinnen, M. Bresselge, K. Vandewal, L. Goris, and J. Manca, "Nanoscale electrical characterization of organic photovoltaic blends by conductive atomic force microscopy," *Appl. Phys. Lett.* **89**, 032107 (2006).
53. R. A. Marsh, C. R. McNeill, A. Abrusci, A. R. Campbell, and R. H. Friend, "A unified description of current–voltage characteristics in organic and hybrid photovoltaics under low light intensity," *Nano Lett.* **8**, 1393–1398 (2008).
54. O. G. Reid, K. Munechika, and D. S. Ginger, "Space charge limited current measurements on conjugated polymer films using conductive atomic force microscopy," *Nano Lett.* **8**, 1602–1609 (2008).

55. J. Nelson, J. Kirkpatrick, and P. Ravirajan, "Factors limiting the efficiency of molecular photovoltaic devices," *Phys. Rev. B* **69**, 035337 (2004).
56. A. Kumar, S. Sista, and Y. Yang, "Dipole induced S-shaped I-V curves in polymer solar cells," *J. Appl. Phys.* **105**, 094512 (2009).
57. A. Wagenpfahl, D. Rauh, M. Binder, C. Deibel, and V. Dyakonov, "S-shaped current-voltage characteristics of organic solar cell," *Phys. Rev. B* **82**, 115306 (2010).
58. A. Kumar, G. Li, Z. Hong, and Y. Yang, "High efficiency polymer solar cells with vertically modulated nanoscale morphology," *Nanotechnology* **20**, 165202 (2009).
59. C. R. McNeill, S. Westenhoff, C. Groves, R. H. Friend, and N. C. Greenham, "Influence of nanoscale phase separation on the charge generation dynamics and photovoltaic performance of conjugated polymer blends: Balancing charge generation and separation," *J. Phys. Chem. C* **111**, 19153–19160 (2007).

Biographies and photographs of the authors not available.